

Numerical Simulation of Hurricane Bonnie (1998). Part II: Sensitivity to Varying Cloud Microphysical Processes

TONG ZHU* AND DA-LIN ZHANG

Department of Atmospheric and Oceanic Science, University of Maryland, College Park, College Park, Maryland

(Manuscript received 24 October 2003, in final form 13 October 2004)

ABSTRACT

In this study, the effects of various cloud microphysics processes on the hurricane intensity, precipitation, and inner-core structures are examined with a series of 5-day explicit simulations of Hurricane Bonnie (1998), using the results presented in Part I as a control run. It is found that varying cloud microphysics processes produces little sensitivity in hurricane track, except for very weak and shallow storms, but it produces pronounced departures in hurricane intensity and inner-core structures.

Specifically, removing ice microphysics produces the weakest (15-hPa underdeepening) and shallowest storm with widespread cloud water but little rainwater in the upper troposphere. Removing graupel from the control run generates a weaker hurricane with a wider area of precipitation and more cloud coverage in the eyewall due to the enhanced horizontal advection of hydrometeors relative to the vertical fallouts (or increased water loading). Turning off the evaporation of cloud water and rainwater leads to the most rapid deepening storm (i.e., 90 hPa in 48 h) with the smallest radius but a wider eyewall and the strongest eyewall updrafts. The second strongest storm, but with the most amount of rainfall, is obtained when the melting effect is ignored. It is found that the cooling due to melting is more pronounced in the eyewall where more frozen hydrometeors, especially graupel, are available, whereas the evaporative cooling occurs more markedly when the storm environment is more unsaturated.

It is shown that stronger storms tend to show more compact eyewalls with heavier precipitation and more symmetric structures in the warm-cored eye and in the eyewall. It is also shown that although the eyewall replacement scenarios occur as the simulated storms move into weak-sheared environments, the associated inner-core structural changes, timing, and location differ markedly, depending on the hurricane intensity. That is, the eyewall convection in weak storms tends to diminish shortly after being encircled by an outer rainband, whereas both the cloud band and the inner eyewall in strong storms tend to merge to form a new eyewall with a larger radius. The results indicate the importance of the Bergeron processes, including the growth and rapid fallout of graupel in the eyewall, and the latent heat of fusion in determining the intensity and inner-core structures of hurricanes, and the vulnerability of weak storms to the influence of large-scale sheared flows in terms of track, inner-core structures, and intensity changes.

1. Introduction

It has long been recognized that cloud microphysical processes play an important role in the triggering, organization, and development of mesoscale convective systems (MCSs). Fujita (1959) speculated that the melting and evaporative cooling could be responsible for

the production of mesoscale high pressure perturbations characterized by divergent flows near the surface. Riehl (1969) and Zipser (1969) hypothesized that evaporative cooling could initiate and maintain mesoscale downdrafts underneath precipitating stratiform clouds. Leary and Houze (1979) indicated the effects of melting on the generation of mesoscale downdrafts in MCSs. Simpson et al. (1965) suggested that cloud seeding in updraft regions increases buoyancy through additional latent heat release of fusion and sublimation.

Mesoscale and cloud-resolving numerical models have also shown the importance of various microphysical processes in simulating the intensity and structures of MCSs. Using a two-dimensional (2D) model, Brown (1979) demonstrated that cloud evaporative cooling

* Current affiliation: CIRA, Colorado State University, Fort Collins, Colorado.

Corresponding author address: Dr. Da-Lin Zhang, Dept. of Atmospheric and Oceanic Science, University of Maryland, College Park, College Park, MD 20742-2425.
E-mail: dalin@atmos.umd.edu

could induce mesoscale downdrafts beneath the anvil clouds. With a mesoscale hydrostatic model, Zhang (1989) studied the sensitivity of the simulated MCSs associated with the July 1977 Johnstown flood to a two-class (cloud ice and snow) ice microphysics scheme. He found that freezing and depositional growth assist the development of a midlevel warm-core vortex, while the subcloud-layer melting weakens the concentration of cyclonic vorticity and its associated low pressure system in the lower troposphere. Meanwhile, the resolvable-scale precipitation begins to develop nearly 1 h earlier and undergoes a more rapid acceleration when the ice microphysics is incorporated. In a numerical sensitivity study of an intense squall line, Zhang and Gao (1989) found that numerical simulations without ice microphysics produce considerably weak descending rear inflow and surface pressure perturbations but too-strong upward motion in the squall system. McCumber et al. (1991) compared cloud-resolving simulations of idealized tropical convection with three different ice physics options: no ice, a two-class, and a three-class (i.e., ice, snow, and graupel) ice scheme. They found that the three-class ice scheme produces more realistic results than those with the other two schemes. Zhang and Fritsch (1988) and Zhang et al. (1994) showed that incorporation of parameterized moist downdrafts and resolvable-scale cooling processes could help alleviate the development of spurious and intense grid-scale mesocyclones, and reproduce more realistically many inner-core structures and evolution of MCSs.

Although numerical studies of tropical cyclones originated in early 1960s, more realistic simulations of the inner-core structures of hurricanes, using more sophisticated cloud microphysics models, only began in the past few years (see the related review by Liu et al. 1997). Earlier explicit simulations of tropical cyclones used axisymmetric warm-rain cloud models (Yamasaki 1977; Rosenthal 1978). Explicit hurricane simulations have now been performed using three-class ice microphysics schemes with the grid sizes of 1.5–6 km (e.g., Liu et al. 1997; Braun and Tao 2000; Wang 2001; Yau et al. 2004).

Unlike the many observational and modeling studies of midlatitude MCSs, few studies have been conducted to investigate the effects of different cloud microphysical processes on the simulation of hurricane intensity and inner-core structures. Most of the currently used cloud microphysics schemes were developed in 1970s based on observations and theories for midlatitude MCSs. There still appear to be many uncertainties in cloud microphysics parameterizations used for hurricane models. Using an axisymmetric nonhydrostatic hurricane model, Lord et al. (1984) found that the use

of a three-class ice scheme produces more realistic structures and evolution of an idealized tropical cyclone, as compared to a no-ice simulation. Although the simulated storm with an ice phase scheme develops slowly during the first two days, its minimum sea level pressure is about 40% deeper than that with a warm-rain scheme after 100 h. They confirmed that cooling due to the melting of ice particles can initiate and maintain downdrafts on a scale of few tens of kilometers, and hypothesized that the downdrafts contribute to the formation of multiple convective rings. Recently, Wang (2002) conducted a series of sensitivity simulations with idealized initial conditions to study the effects of varying cloud microphysics processes on tropical cyclones. He showed that hurricane intensity and inner-core structures change markedly when different cloud physics processes are included. Of interest is that the warm-rain microphysics scheme tends to generate a fast intensifying storm with a stronger final intensity than that with the mixed-phase cloud scheme. This result appears to contradict the finding of Lord et al. (1984). Wang attributed this rapid intensifier to the development of weak moist downdrafts in the absence of ice physics processes. Because of the use of idealized initial conditions with little vertical shear and because of the use of the two different hurricane models in the above-mentioned studies, it is uncertain which of the above findings is valid and applicable to tropical cyclones in nature.

Thus, the purposes of this study are to (a) examine the effects of various cloud microphysics processes on the intensity change, precipitation, and inner-core structures of Hurricane Bonnie (1998), and (b) gain insight into the inner-core structural changes of hurricanes with different intensities as they interact with the same larger-scale sheared environment. This will be done through a series of high resolution ($\Delta x = 4$ km) sensitivity simulations using a two-way interactive, triply nested (36/12/4 km), movable-grid version of the nonhydrostatic, cloud-resolving fifth-generation Pennsylvania State University–National Center for Atmospheric Research (PSU–NCAR) Mesoscale Model (MM5; Dudhia 1993; Grell et al. 1995).

The next section summarizes briefly the control simulation and describes the model design of the sensitivity simulations. Section 3 presents the sensitivity of the model-simulated storms to various cloud microphysics processes in terms of track, intensity, and precipitation. Section 4 shows their impact on the simulated inner-core structures, particularly the wavenumber-1 asymmetries and eyewall replacement scenarios. A summary and concluding remarks are given in the final section.

TABLE 1. Summary of the experimental design.

Experiment	Description
CTL	Control simulation with the Tao–Simpson three-ice microphysics scheme
NEVP	As in CTL but without the evaporation of rain and cloud water
NMLT	As in CTL but without the melting of ice, snow, and graupel
NGP	As in CTL but without the graupel phase
NICE	As in CTL but without ice microphysics variables
NICE2	As in NICE but with the addition of latent heat of fusion for phase changes occurring below the temperature of 0°C (i.e., above the melting level)

2. Experimental design

In Part I of this series of papers, Zhu et al. (2004) showed a 5-day control simulation (CTL) of Hurricane Bonnie (1998) with the MM5 that covers the initial rapid deepening, steady variation and landfalling stages of the storm. As described in Zhu et al. (2002), the initial hurricane vortex is retrieved mostly from the Advanced Microwave Sensing Unit-A (AMSU-A) data, with some surface parameters specified from the Third Convection and Moisture Experiment (CAMEX-3) observations. The model initial conditions and lateral boundary conditions are obtained from the National Centers for Environmental Prediction (NCEP) 2.5° × 2.5° global analysis. The sea surface temperature (SST) is updated daily using the Tropical Rainfall Measuring Mission (TRMM) Microwave Imager (TMI) Level 1 (IB11) standard product (Chelton et al. 2000). The model physics used in the finest 4-km resolution domain include the Tao–Simpson (1993) three-class ice [i.e., cloud ice (q_i), snow (q_s), and graupel (q_g)] and cloud [i.e., cloud water (q_c) and rainwater (q_r)] microphysics scheme, the Blackadar planetary boundary layer (PBL) scheme (Zhang and Anthes 1982), and a radiation scheme. The Tao–Simpson scheme contains prognostic equations for cloud water and ice, rainwater, snow, and graupel, and it allows for the generation of supercooled water.

It was shown that the 5-day control simulation reproduces reasonably well the track, intensity change and asymmetric inner-core structures of the storm, including a partial eyewall and an eyewall replacement cycle (Zhu et al. 2004). In this study, five sensitivity experiments (see Table 1) are designed to examine the effects of cloud microphysics parameterizations on the hurricane intensity and intensity changes, and the development of cloud and rainfall asymmetries as well as the eyewall replacement scenarios, by modifying different routines of the Tao–Simpson (1993) cloud microphysics scheme. In the first experiment, the prognostic equations of cloud ice, snow, and graupel are excluded from the control simulation (NICE), namely, only the warm-

rain physics is allowed. To minimize the initial differences in phase-change rates, the initial 3D relative humidity field, calculated with ice saturation for the water vapor above the 0°C layer, is kept identical between the CTL and NICE experiments. This simulation is similar to the warm-rain scheme used by Willoughby et al. (1984), Lord et al. (1984), and Wang (2002). In the second experiment, the prognostic equation for graupel is removed from the control run (NGP). In addition, we have removed the wet and dry growth of graupel from cloud water, rainwater, cloud ice, and snow, as well as the autoconversion (aggregation) of snow to graupel and the freezing of rainwater into graupel. Because of no graupel production, its associated melting and sublimation will not be seen. These two sensitivity simulations are designed to examine to what extent the simulated hurricane intensity and structures are directly affected by the incorporation of ice microphysics. Exclusion of the ice microphysics implies the neglect of three phase interchanges, latent heat of fusion, and fall-out, thus modifying the vertical profiles of latent heating and water loading in the eyewall updrafts.

In the third experiment, the melting of ice, snow, and graupel to form rainwater as falling through the 0°C isothermal layer is neglected, so the associated cooling and phase change effects are absent (NMLT). In the fourth experiment, evaporation of cloud water and rainwater in subsaturated regions are turned off from the control simulation (NEVP). These two experiments are designed to investigate the roles of melting and evaporative cooling in determining the intensity of tropical cyclones, and they are also closely related to ice microphysical processes.

3. Impact on hurricane intensity

Since hurricane intensity depends highly on the magnitude and distribution of latent heat release, it is desirable to examine first the different vertical structures of cloud hydrometeors as various ice microphysics processes are downgraded from the control simulation. The vertical hydrometeor structures may provide in-

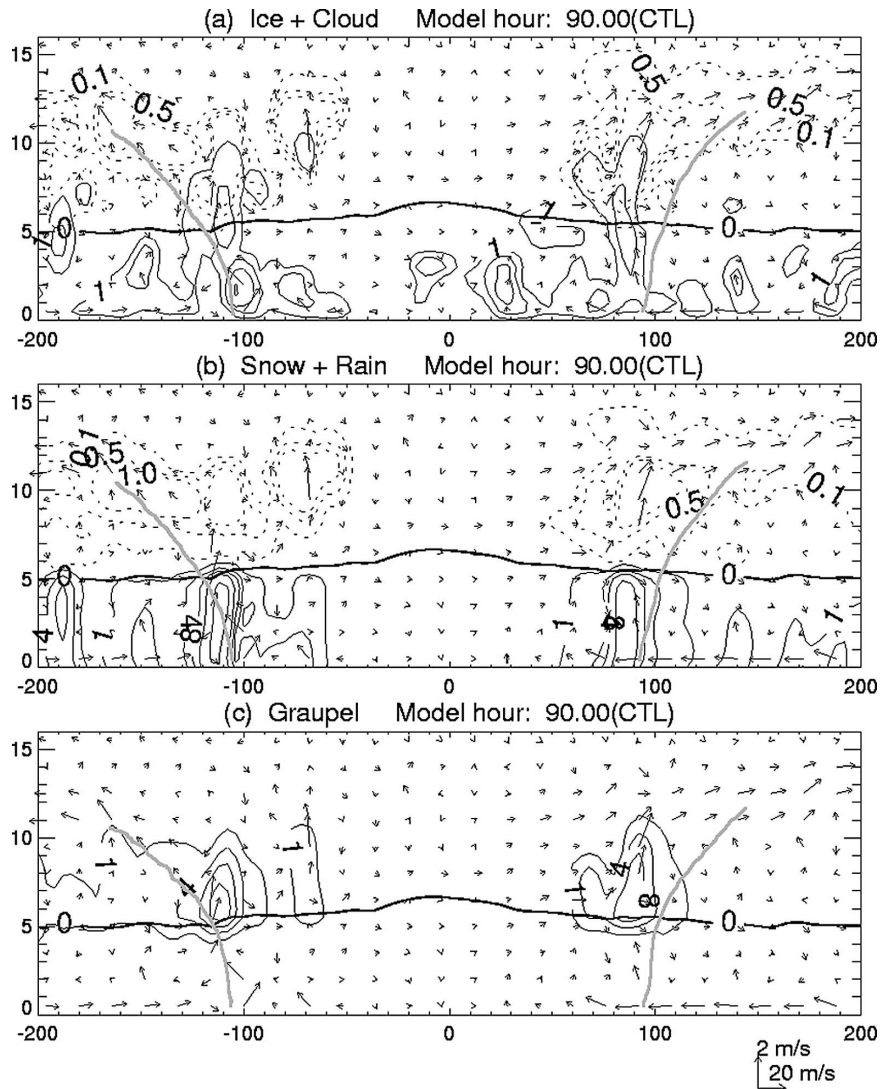


FIG. 1. East-west vertical cross sections, through the hurricane center, of the mixing ratios at intervals of $10^{-4} \text{ kg kg}^{-1}$ of (a) cloud water (solid) and cloud ice (dashed), (b) rainwater (solid) and snow (dashed), and (c) graupel which are taken from the 90-h CTL simulation. The in-plane storm-relative flow vectors are superimposed. The heavy and light solid lines denote the distribution of the 0°C isotherm and the RMW, respectively.

sight into the mechanisms by which precipitation and certain inner-core flows are generated.

a. Vertical structures of hydrometeors

Figure 1 shows the west-east vertical cross sections of the mixing ratios of hydrometeors through the hurricane center at 90 h into the control simulation, when the storm enters an azimuthally near-symmetric stage. Cloud water is based as low as 100 m and it extends up to 10 km in the form of supercooled water. Cloud ice and snow are concentrated in the upper outflow stratiform regions with the maximum near $z = 10 \text{ km}$. They

grow by freezing of supercooled water, deposition of water vapor, and in response to the latent heat release in updrafts

Unlike the cloud ice and snow, graupel is concentrated primarily in strong updrafts (i.e., $>1 \text{ m s}^{-1}$) in the eyewall, and it melts into rainwater as falling through the 0°C layer. Because of the efficient accretion process, less snow appears in the 2–3-km layer above the melting level where graupel (and updrafts) is peaked (cf. Figs. 1b and 1c). The magnitude and distribution of all the hydrometeors are similar to those found in other model simulations (Lord et al. 1984; Liu

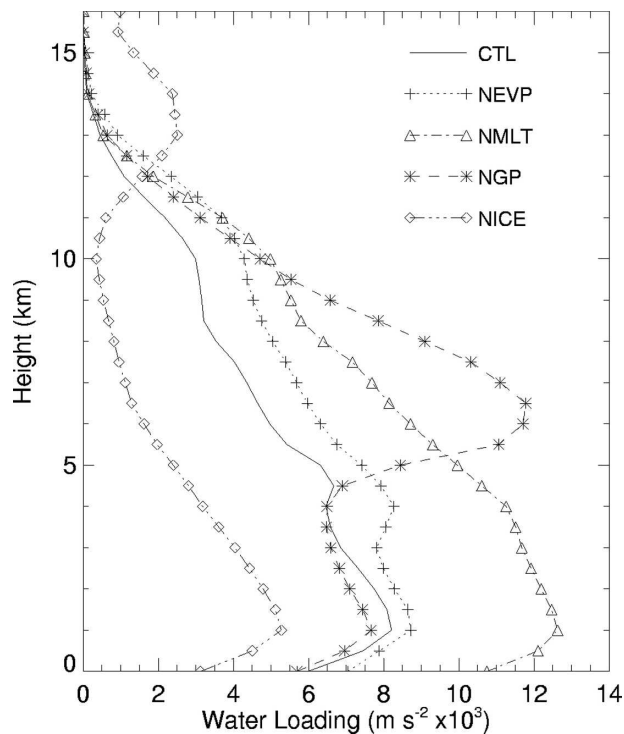


FIG. 2. Vertical profiles of the water loading [$g(q_i + q_s + q_e + q_c + q_r)$] that are averaged over an area of $250 \text{ km} \times 250 \text{ km}$ centered at the hurricane's surface minimum pressure from the five 90-h sensitivity simulations.

et al. 1997; Wang 2002). The area-averaged vertical profile of the total cloud hydrometeors (or water loading) displays an increase with the updraft intensity in the lowest 1-km layer, and a general decrease with height above as more fallout occurs (Fig. 2). As shown in Zhu et al. (2002, 2004), the distribution and magnitude of the simulated radar reflectivity, which is an integrated variable of all cloud hydrometeors, compare favorably to those observed during CAMEX-3.

Without the evaporation of cloud water and rainwater (NEVP), the radius of maximum wind (RMW) shrinks, with stronger and more slantwise updrafts in the eyewall (cf. Figs. 1b and 3a). Of relevance is the increased (eyewall) width of rainwater and its upright distribution outside the RMW that result clearly from no evaporation of falling rainwater in the subcloud unsaturated layers. Moreover, because of the more rapid fallout after the phase change from ice to liquid, the total cloud hydrometeors content decreases in the melting layer (i.e., below $z = 4 \text{ km}$) in both NEVP and CTL (Fig. 2).

Similarly, graupel in NMLT could fall to the surface because of the neglect of melting, leading to the generation of wider and more upright precipitation regions in the eyewall (cf. Figs. 1c and 4). Updrafts are also

much stronger than those in CTL, and become more favorable for the production of graupel in the eyewall. The enhanced updrafts in NEVP and NMLT appear to result from a positive feedback between the low-level convergence of relatively warmer and more moist air, the latent heat release in the eyewall, and surface pressure falls. Note the more pronounced water loading below $z = 4 \text{ km}$ in NMLT (Fig. 2) that appears to result from more rapid depositional growth and accretion of snow and graupel in the moisture-rich submelting layer.

In the absence of graupel (NGP), a wider lateral cloud band of the eyewall is generated as snow is more radially advected than vertically relative to graupel (cf. Figs. 3b and 1b). Because of its smaller terminal velocity and no conversion to graupel, an unusual amount of snow mixing ratio is distributed above the melting layer (see Figs. 2 and 3b), and peaked near the core of updrafts supporting its growth. It is likely that because of the increased water loading, the eyewall updrafts are not as strong as those in CTL, particularly near the peak hydrometeors level where convective updrafts are often maximized. This result indicates the importance of incorporating graupel in reducing the water loading in the eyewall updrafts and in obtaining a more realistic vertical profile of cloud hydrometeors.

Without allowing the presence of ice particles (NICE), cloud water is widespread in the upper troposphere, floating with the mean flow (cf. Figs. 5 and 1a). But little rainwater could be generated above the 0°C isothermal level, because the mixing ratio of cloud water is too small to reach the threshold value (i.e., 0.5 g kg^{-1}) for being converted to rainwater (cf. Figs. 3c and 1b). Clearly, the absence of the latent heat release of fusion and the initiation of cloud ice from water vapor for $T < 0^\circ\text{C}$ would retard the production of cloud water, as will be seen in terms of intensity in the next subsection, and its subsequent autoconversion and accretion processes would be much slower than those associated with snow and graupel as well as their depositional growth process in ice microphysics. Thus, the model produces the weakest and shallowest hurricane vortex with the largest RMW among all the simulations conducted (cf. Figs. 1 and 3–5). Comparing the results among CTL, NGP, and NICE, we may state that the presence of graupel helps narrow the lateral eyewall dimension due to its rapid fallout, while the latent heat of fusion plays a primary role in intensifying the eyewall updrafts in the CTL storm. In nature, graupel could only develop in strong updraft regions because of a long time required for the growth of an ice particle to a diameter of 5 mm and larger. As will be seen in the next few subsections, the above results have different implications with respect to the intensity and intensity

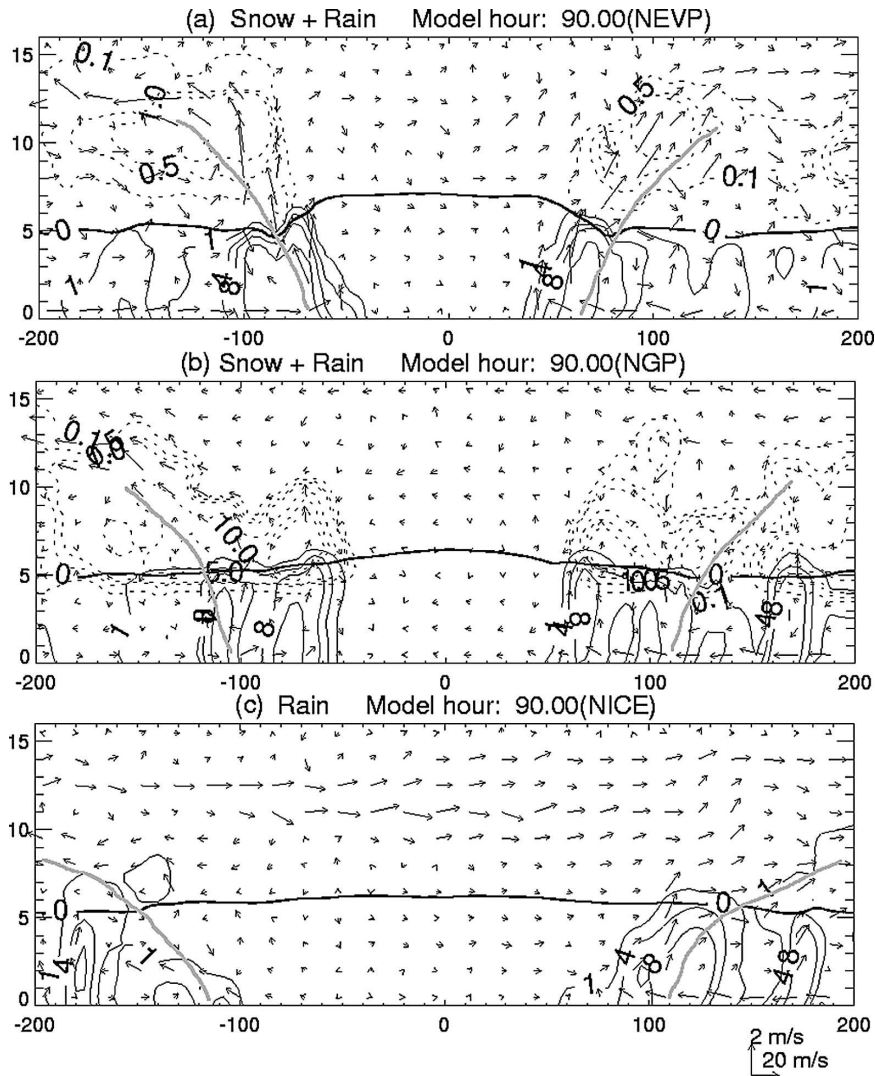


FIG. 3. As in Fig. 1b but from (a) NEVP, (b) NGP, and (c) NICE.

change as well as the inner-core structures of the simulated hurricanes.

b. Hurricane tracks and intensity

Figure 6 shows that all the sensitivity-simulated tracks resemble the control-simulated and the observed, except for the NICE storm that does not make landfall. The NICE track is similar to most of the then operational forecasts initialized on 22 and 23 August 1998, showing that Bonnie was going to remain out to sea (see Avila 1998). Because the hurricane movement is mainly determined by a deep-layer-averaged environmental flow, the north-to-northeastward shift of the NICE track after 60 h into the integration indicates more influences of the midlatitude westerly flow on the steering of the storm. Since the NICE storm is the

weakest and shallowest one among the simulated (see Figs. 1, 3, and 7), this result appears to suggest that weaker (and shallower) hurricanes tend to be more vulnerable to the influence of large-scale flows. This is clearly evidenced by the presence of (system relative) westerly (sheared) flows in the upper troposphere (i.e., above $z = 9$ km) of the NICE storm (see Fig. 3c).

Figure 7 compares the time series of the simulated minimum central pressure (P_{\min}) and maximum surface wind (V_{\max}) from the sensitivity experiments to the control simulated. Pronounced differences (or sensitivity) in hurricane intensity from the control simulation are evident between 24 and 102 h into the integration, with the extreme amplitudes ranging from 50 hPa (or 20 m s^{-1}) overdeepening to 10 hPa (or 12 m s^{-1}) underdeepening in P_{\min} (V_{\max}). Note that all the storms

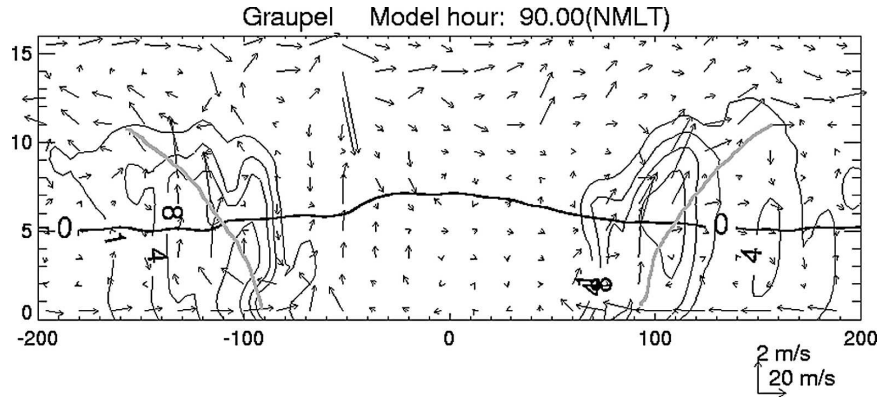


FIG. 4. As in Fig. 1c but from NMLT.

deepen in coincidence with the rapid increase in vertical wind shear as they move toward a midlatitude upper-level disturbance (see Zhu et al. 2004). Despite the large differences in intensity, nearly all the storms begin to weaken after 3 days as they move over a colder water surface and approach the east coast. Subsequently, they gradually converge to the control simulated, and all are eventually absorbed by the large-scale mean flows.

It is apparent from Fig. 7a that the NICE storm experiences the weakest development with the minimum central pressure of 963 hPa at 69 h, as compared to the CTL-simulated 954 hPa. This result is similar to that obtained by Willoughby et al. (1984) and Lord et al. (1984) using an axisymmetric cloud model, but it differs from the idealized simulations of tropical cyclones by Wang (2002) in which the warm-rain scheme produces a stronger storm than that when the three-ice scheme is used, as mentioned before. His results also show little sensitivity between the simulations with and without ice microphysics, and between the simulations using different fall velocities of graupel; all of these are in significant contrast with the results presented herein (cf. Fig. 7 herein and Fig. 2 in Wang 2002). These differences may be attributed to the different physical processes

incorporated in these two different models, if not to the different (sheared) environments in which the storms are embedded. Clearly, a model intercomparison study is warranted in order to understand how these differences arise.

In the present case, more significant departures between the CTL and NICE storms begin after 36 h, as the CTL storm spins up with more latent heat release of fusion and generation of more graupel in the eyewall updrafts. To examine the effects of including the latent heat of fusion on the cyclogenesis, another experiment is conducted, in which additional heating of fusion (i.e., $L_f = 3.336 \times 10^5 \text{ J kg}^{-1}$) is incorporated into NICE for the phase changes taking place in the layers above the melting level (NICE2). This modification increases the magnitude of latent heating (cooling), with respect to NICE, wherever condensation (evaporation) occurs above the 0°C isothermal level. As a result, the simulated storm is about 18-hPa deeper than the NICE-simulated one, and even 8 hPa deeper than the CTL storm. The latter is most likely because of the neglect of melting, as can be seen by comparing CTL and NMLT, which will be described later.

Adding the ice microphysics scheme into NICE but

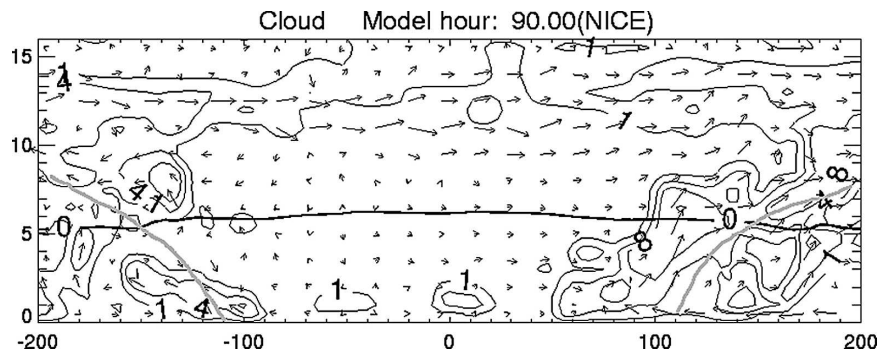


FIG. 5. As in Fig. 1a but from the NICE simulation.

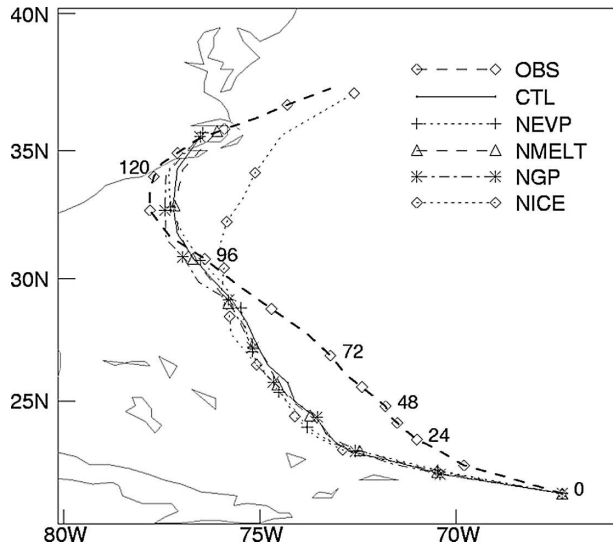


FIG. 6. Six-hourly tracks of Hurricane Bonnie from the best analyses (thick solid) and the model simulations.

without graupel (NGP) improves the intensity simulation, more significantly after 72 h (Fig. 7a). This results mostly from the added heating associated with freezing and depositional growth, as partially shown in NICE2. The negative impact of melting on the intensity appears to be secondary partly because of its occurrence more inside the RMW (Fig. 3b) where less mass is entrained into the eyewall updrafts. Adding graupel to NGP gives the more realistic simulation of the CTL storm. The asymptotic improvement from NICE to NGP and CTL is consistent with that obtained during the initial experimental simulations of Hurricane Andrew (1992), [see, e.g., Fig. 7 in Zhang (1998)]. Since the introduction of graupel into CTL is to increase the fallout of hydrometeors with respect to snow, the inclusion of graupel tends to reduce the water loading effects on the eyewall updrafts (Fig. 2), leading to the intensification of the vortex rotation. The water loading effects appear to be more pronounced after the 42-h integration when more graupel is generated, as indicated by the increasing departures in P_{\min} between CTL and NGP (Fig. 7a). The inclusion of graupel helps reproduce more realistically the intensity change near the end of Bonnie's rapid deepening stage (i.e., near $t = 48$ h; see Zhu et al. 2004).

In the absence of both the cloud water and rainwater evaporation (NEVP) or the melting of cloud ice particles (NMLT), the storm undergoes extremely rapid intensification in the first 2–3 days, as compared to the control simulation. The NEVP storm deepens more than 85 hPa in 2 days, at a rate of about 1.8 hPa h^{-1} , which has rarely been reported in the literature. The

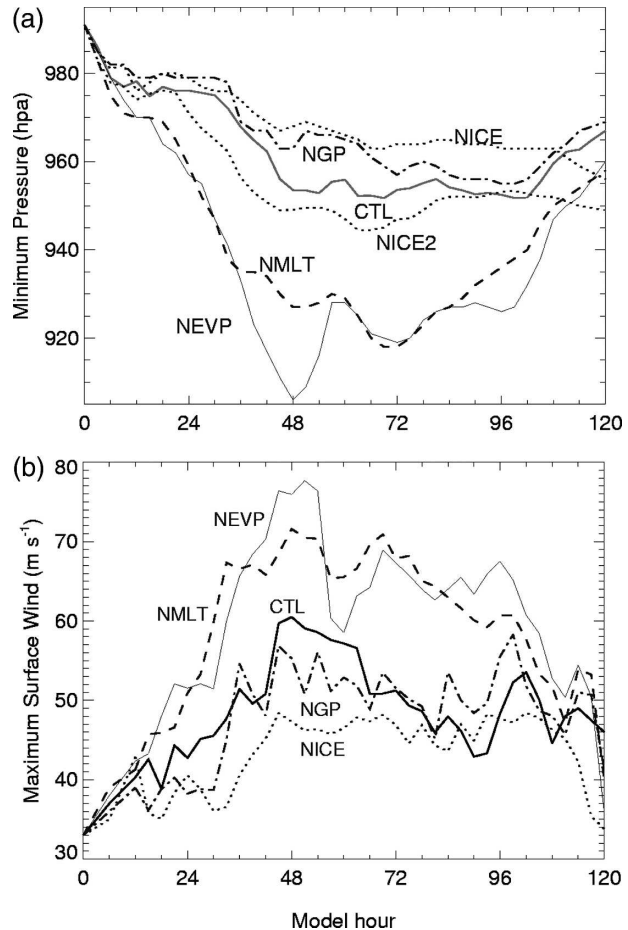


FIG. 7. Three-hourly time series of (a) the minimum central pressure (P_{\min} , hPa) and (b) the maximum surface wind (V_{\max} , m s^{-1}) for all the model simulations.

NMLT storm has a time series of P_{\min} that is similar to the NEVP storm except for the 36–60-h period. Similar scenarios occur in the idealized simulations of Wang (2002), despite that some different processes are excluded in his NMLT and NEVP runs. For example, because the evaporative cooling is also removed in his NMLT run, the resulting cyclone is systematically much stronger than that in NEVP. In the present case, the comparable intensities of the NMLT and NEVP storms suggest that the cooling effects of melting ice particles are similar to those of evaporating cloud and rainwater on “braking” the development of a hurricane. This could be explained by the fact that little evaporative cooling could occur in a near-saturated environment, particularly in the core of the eyewall, whereas the strong melting cooling often occurs in a close proximity vertically within the regions of intense latent heat release (in the core of the eyewall).

In general, the time series of V_{\max} and its rates of

changes coincide well with those of P_{\min} , but showing more pronounced fluctuations (cf. Figs. 7a and 7b). These fluctuations appear to be caused partly by the structural changes in inner-core mean flows and partly by some propagating waves, such as vortex–Rossby waves (Montgomery and Kallenbach 1997) and/or gravity-inertial waves (Willoughby 1978; Liu et al. 1999). Note that the magnitude of V_{\max} does not always correspond to that of P_{\min} when comparing different simulations, for example, between CTL and NGP during the 81–99-h simulations, and between NEVP and NMLT during the 24–36- and 54–84-h simulations. Similar scenarios occur in the simulations of Willoughby et al. (1984) and Lord et al. (1984), in which the same maximum wind of about 45 m s^{-1} is reached but with a final 18-hPa difference in P_{\min} , when two different microphysics schemes are used. This is because the simulated V_{\max} , unlike that in the best analysis, is a point value that could be locally determined by deep convection, whereas P_{\min} may be roughly considered as a system-integrated quantity.

c. Vertical heating profiles

To help gain insight into the sensitivity of the simulated storm intensities to various cloud microphysical processes shown in the preceding subsection, we examine their associated vertical heating profiles that play an important role in determining the rates of cyclogenesis. With the hourly model output of potential temperature (θ), the diabatic heating rates ($d\theta/dt$) can be estimated by

$$\frac{d\theta}{dt} = \frac{\partial\theta}{\partial t} + u \frac{\partial\theta}{\partial x} + v \frac{\partial\theta}{\partial y} + w \frac{\partial\theta}{\partial z}, \quad (1)$$

in which the advective effects associated with the storm translation are retained but the local tendencies in the storm-relative coordinates are neglected, based on the budget study of Zhang et al. (2002). The latter should be extremely small near the 90-h integration when all the storms enter a mature and near-axisymmetric stage.

Figure 8 shows various (storm-scale averaged) vertical heating profiles from the 90-h sensitivity simulations to the control simulated. All the heating profiles show an increase in the heating rates in the PBL and a deep layer of constant heating in the layer of $z = 1\text{--}5 \text{ km}$, except for the NMLT profile, with bifurcating profiles above. A comparison of the NMLT profile to the others reveals the significance of melting in reducing the heating rates in the lower troposphere, thereby limiting the deepening of the storms. Without the melting effect, the storm-scale heating rates increase from 6°C h^{-1} at $z = 0.5 \text{ km}$ to 12°C h^{-1} at $z = 6 \text{ km}$; the peak rate more

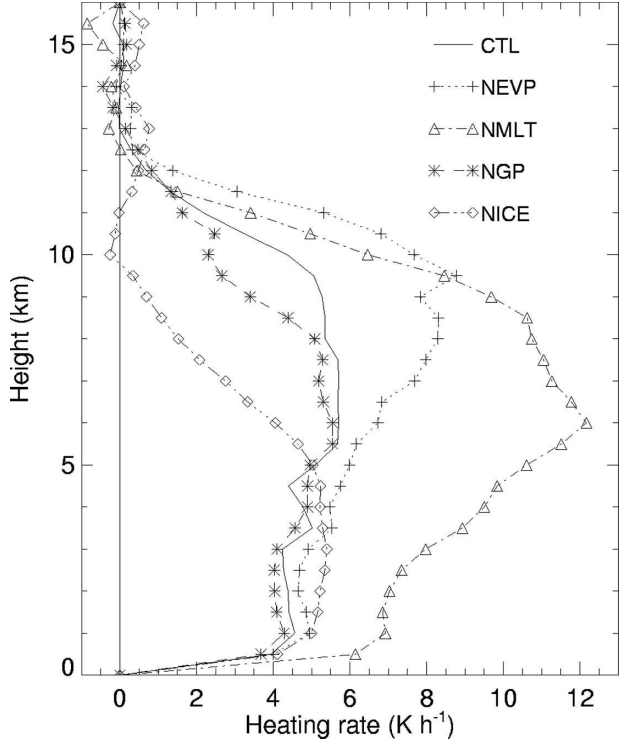


FIG. 8. As in Fig. 2, but for the diabatic heating rates ($d\theta/dt$, K h^{-1}).

than doubles that in CTL, NGP, and NICE. The rapid drop in heating rates below $z = 6 \text{ km}$ appears to be closely associated with the increased water loading effect that weakens part of the eyewall updrafts (see the NMLT profiles in Figs. 2 and 8). Of importance is that this melting effect is much more significant than the evaporative cooling, as can be seen by comparing the NEVP–CTL and NMLT–CTL heating profiles, since the air in the eyewall, where heavy rainfall occurs, is nearly saturated. However, the development of the deepest NEVP storm suggests that evaporation of cloud hydrometeors play a more important role than the melting of ice particles in suppressing the cyclogenesis in the first two days when the adjacent environment is more unsaturated and less graupel and precipitating snow are available for melting. Subsequently, the evaporative cooling decreases as the environmental moisture field spins up, and becomes less than the melting effects as more graupel is generated in more intense updrafts for melting.

Of interest is the development of an inversion in heating rates between 4.5 and 6 km in the CTL profile, which is indicative of the freezing above the melting below. The melting layer is less pronounced in the NGP profile, suggesting the significance of melting graupel and incorporating graupel into the cloud ice microphys-

ics scheme in determining the vertical heating profile. As shown in Zhu et al. (2004), this melting effect accounts for a temperature inversion in the melting layer in a sounding taken in the eyewall (see Fig. 5b therein). As indicated by many previous studies (e.g., Riehl 1969; Leary and Houze 1979; Brown 1979; Zhang and Gao 1989), the melting (and evaporative) cooling, though occurring locally in a shallow layer, could initiate penetrative mesoscale downdrafts that transport the midlevel low- θ_e air to the PBL, thereby stabilizing the atmospheric columns or suppressing updrafts in the eyewall.

Above the melting layer, the heating profiles show more pronounced sensitivity to different cloud physical processes (Fig. 8). Without the latent heating of fusion through freezing and depositional growth, the heating rates in NICE decrease rapidly above $z = 5$ km, which is consistent with the presence of the weakest updrafts in the upper eyewall (cf. Figs. 5 and 8). Adding a two-ice (i.e., cloud ice and snow) microphysics scheme into NICE improves significantly the upper portion of the vertical heating profiles (i.e., see NIC, NGP, and CTL) and the eyewall updrafts (cf. Figs. 1b, 3b, and 5) as well as the intensity simulation (cf. Figs. 7 and 8). Again, these results differ from those given in Wang (2002), in which greater heating rates are generated above the melting level in NICE than those in CTL. In the present case, incorporating graupel into the model tends to accelerate the latent heat release of fusion aloft because the depositional growth of graupel is a faster process than that of snow (i.e., see the NGP and CTL profiles).

While the effects of evaporative cooling are small below the 0°C isothermal level, removing the evaporative cooling of supercooled water from the CTL run increases the heating rates aloft and shifts the heating maximum to a level 2–3 km higher (i.e., see the CTL and NEVP profiles). Based on the heat budgets of Zhang et al. (2002), the evaporative cooling tends to occur in the subcloud layer outside the eyewall and in the radial inflows in the eyewall that advect the environmental dry and colder air inward. Zhang et al. (2002) also showed that the diabatic heating rates are nearly balanced by the vertical advective cooling rates, suggesting the similar sensitivity of the simulated vertical motion profiles to the above mentioned cloud microphysical processes.

4. Impact on hurricane structures

Zhu et al. (2004) examined the influence of vertical wind shear on the inner-core structures of the CTL storm. The simulation results showed that the strong westerly flow associated with a midlatitude upper-level

disturbance tends to suppress deep convection in the western semicircle of the eyewall as Bonnie approaches the east coast, leading to the development of wavenumber-1 asymmetries in clouds and precipitation (i.e., a partial eyewall), and the eastward tilt of the eyewall and eye. Both the observed and simulated storms also exhibit an eyewall replacement scenario prior to its landfall in which it weakens as double eyewalls appear, and reintensifies as its inner eyewall diminishes and a concentric eyewall develops. It should be mentioned that the eyewall replacement occurs as the storm moves to a weak-sheared environment, which is consistent with the previous observations (e.g., Willoughby et al. 1982). Thus, it is of interest to examine how varying cloud microphysics processes would contribute to these characteristic structural changes.

Figure 9 compares the time–azimuth cross-sections of radar reflectivity through the updraft core in the eyewall at $z = 5$ km between the different simulations. The radius chosen is different for each storm, and is even different for a certain storm at each azimuth angle, because we choose the radius according to the maximum ascending motion. All the model data were then transformed to cylindrical coordinates. First, an azimuthally averaged radius of the maximum updraft was found, and then within ± 5 model grid points (about ± 20 km) of the averaged radius we determined a final radius of the maximum updraft for each azimuth angle. When plotting Fig. 9, we also took a 3-point (12 km) average of the data along the radial direction. The above mentioned wavenumber-1 cloud asymmetries in the first 72 h are apparent in all the simulations, albeit with varying strengths. Although removing graupel allows more cloud hydrometeors to be advected cyclonically, the NGP-simulated precipitation patterns resemble better the CTL simulated among all the sensitivity runs [cf. Fig. 9c herein and Fig. 12 in Zhu et al. (2004)]. That is, most of the clouds and intense precipitation develop in the northeast quadrant, whereas the southwest semicircle is often cloud free. The cloud-free region in CTL is greater than that in NGP because of the rapid fallout of graupel. Similar but weakly organized reflectivity patterns appear in NICE. Although the wavenumber-1 asymmetries also develop in NEVP and NMLT, clouds and precipitation are much more intense and extensive than the other three simulations, with little cloud-free areas in the western eyewall. In particular, the simulated radar reflectivities are peaked in the northern semicircle and decrease in intensity cyclonically downstream, rather than being limited in the northeast quadrant as in CTL and NGP (cf. Figs. 9a–c). Because of more rapid rotational advection of cloud hydrometeors, such wavenumber-1 precipitation structures are less

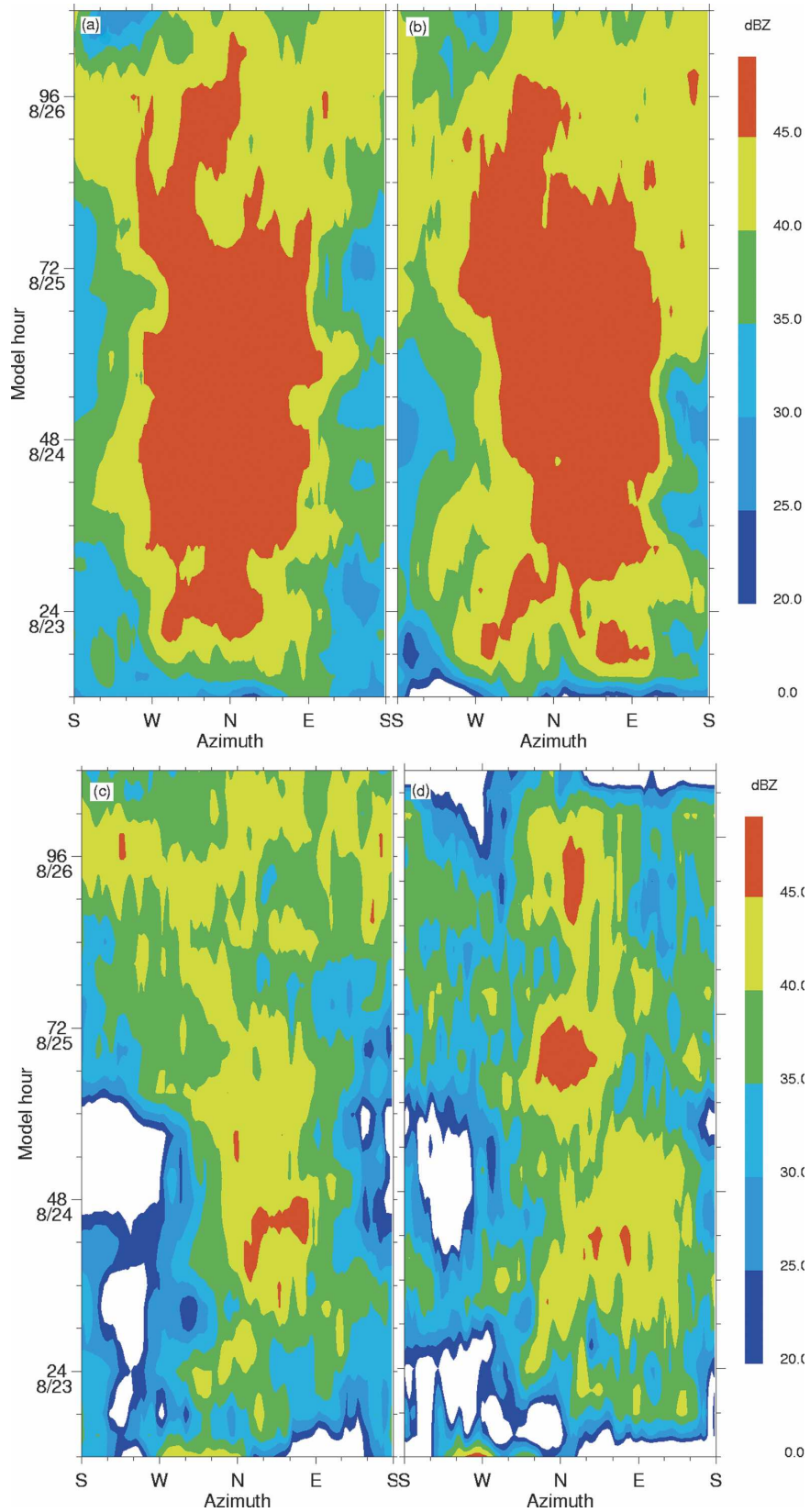


FIG. 9. The time-azimuth cross sections of radar reflectivity along the updraft core at $z = 5$ km from the 5-day simulations of (a) NEVP, (b) NMLT, (c) NGP, and (d) NICE.

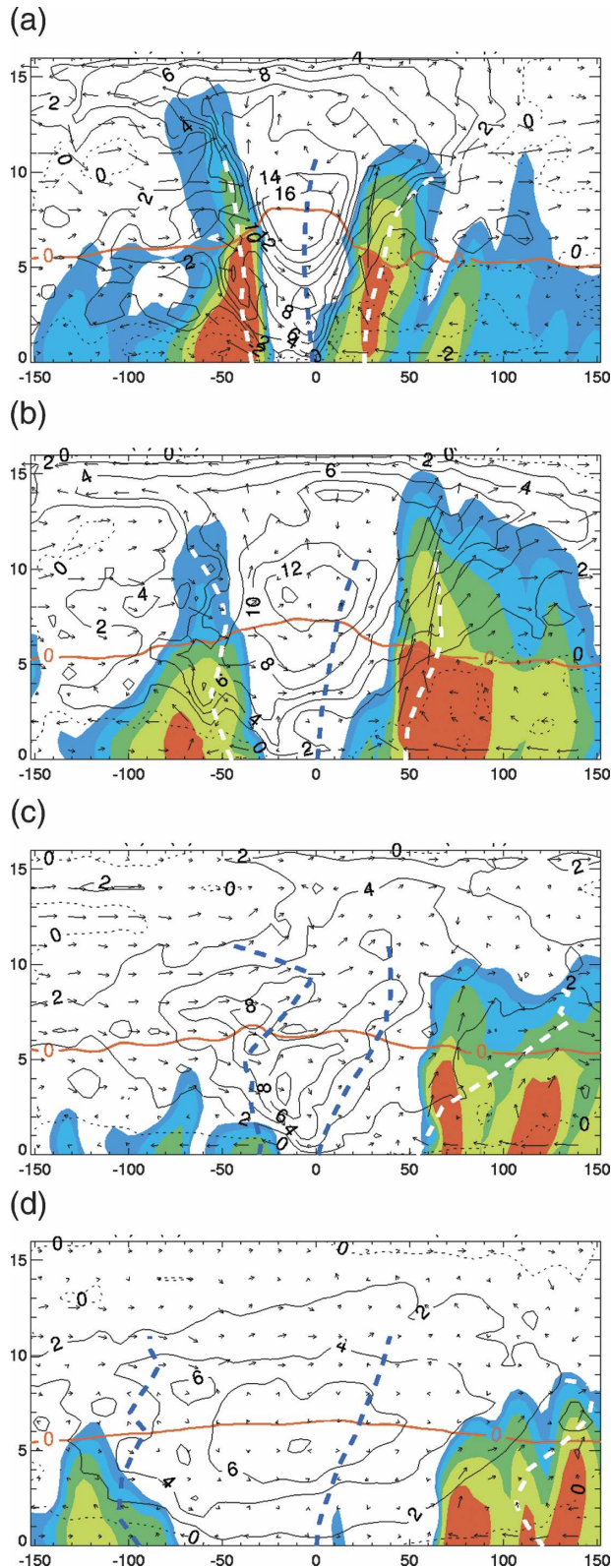


FIG. 10. The west–east vertical cross sections of temperature deviations, at intervals of 2°C , and in-plane flow vectors and radar reflectivity through the eye center from the 48-h simulations for

evident in the layers below $z = 5$ km (not shown). After 72 h, as the environmental vertical shear weakens, precipitating clouds spread quickly to form a near-concentric eyewall. Similar features could also be seen from the observations of National Oceanic and Atmospheric Administration (NOAA)’s WP-3D radar and TRMM surface rainfall rates (not shown). By comparison, although the most intense reflectivity in NEVP and NMLT still remains in the northern semicircle, little cloud-free regions develop in the eyewall as a result of the intense development of rotational flows and eyewall updrafts.

To help gain further insight into the cloud and precipitation asymmetries discussed above, Fig. 10 compares vertical structures of the simulated radar reflectivity, in-plane flow vectors and temperature deviations during the mature stage of the simulated storms. All deviations are obtained by subtracting their layer-averaged values at individual heights. In general, the warm-core intensity is positively (negatively) correlated to the simulated P_{\min} (RMW). The results are consistent with the theory of Zhang et al. (2000) that it is the dynamically induced vertical pressure gradient force (PGF), dominated by the radial shear of V^2 per unit radius, that accounts for the maintenance of a warm core in the eye; where V is the tangential wind. That is, the more rapid rotation with smaller RMW is, the stronger is the downward PGF in the eye. Again, the NGP structures are closer to the CTL simulated [cf. Fig. 10c herein and Fig. 16a in Zhu et al. (2004)]. Specifically, there are little mid-to-upper-level clouds and organized updrafts in the western eyewall, which are in significant contrast to the deep convective development in the eastern eyewall. Moreover, the western RMW and the vertical axis of P_{\min} tilts eastward with the lateral warm centers of over 8°C tilting westward from the surface P_{\min} . These lateral warm centers, differing from typical warm cores in the eye, result from the subsidence warming associated with the upper-level west-to-northwesterly descending inflow (see Zhu et al. 2004).

By comparison, the intense storms simulated in NEVP and NMLT exhibit nearly symmetric vertical structures about the vertical P_{\min} axes except for the in-plane flows (Figs. 10a and 10b). Although the west-to-northwesterly descending inflows generate significant lateral warm perturbations in the western eyewalls, the convectively forced warm cores of $12^{\circ}\text{--}16^{\circ}\text{C}$

(a) NEVP, (b) NMLT, (c) NGP, and (d) NICE. The thick solid and dashed lines denote the distribution of the melting level (i.e., 0°C), the RMW, and the axis of P_{\min} , respectively.

are located at the eye center. This vertical coherent thermal structure appears to be more efficient than the tilted one in CTL and NGP in lowering and maintaining the surface low (cf. Figs. 10 and 7). That is, the more upright the warm core is oriented, the more intense the hurricane vortex would develop. On the other hand, the intense warm-cored eyes in NEVP and NMLT could be well protected from the upper-level northwesterly inflow because their intense rotational flows tend to be stiffer to radial erosion of the environmental flows, as compared to those weaker storms. This could be readily seen by comparing the vertical in-plane flows and thermal structures in Figs. 10a and 10c. Of interest is that in the western portion of the eyewall the midlevel precipitating clouds coincide with the descending inflow, whereas the upper-level clouds are associated with updrafts (see Figs. 10a and 10b). An examination of the height–azimuth cross sections in the eyewall [e.g., Fig. 15 in Zhu et al. (2004)] reveals that the two phenomena are generated by the cyclonic advection of cloud hydrometeors and the upward-cyclonic propagation of updrafts from the northeastern quadrant in the eyewall, respectively. Because of the negative influence of the westerly descending flows, the simulated reflectivities in the western eyewall, as shown in Figs. 9a,b, are much weaker than those in the other quadrants. The above results suggest that the roles of the environmental vertical shear in suppressing cloud development in the eyewall differ in extent, depending upon the intensity of hurricane vortices and the cloud microphysics processes used to predict them.

It is of interest that despite the presence of vertically sheared environment, the symmetric, but much weaker, warm-cored eye structure also develops in NICE, with little lateral warm perturbations in the western eyewall (Fig. 10d). First, the shallow vertical circulation in NICE allows little interaction with the upper-level northwesterly, sheared, lower- θ_e inflow, so little upper-level momentum could be tapped by the storm's secondary circulations. Second, because much less rainwater was available for evaporation (Fig. 3c), little descending motion could develop in the western eyewall so that the lateral warm perturbations are not evident. This indicates that the interaction of cloud microphysics processes with a sheared environment cloud lead to quite different changes in intensity and inner-core structures (cf. Figs. 10a–d). On the other hand, strong storms are less vulnerable to middle to upper-level vertical sheared environments, but their associated secondary circulations could be more highly nonlinear as a result of phase changes.

Figure 11 shows the distributions of accumulated precipitation from all the simulations in order to see how

they correspond to their inner-core cloud structures shown in Figs. 9 and 10. In general, stronger storms tend to be more compact and less asymmetric with heavier rainfall, such as in NEVP and NMLT, whereas the opposite is true for weaker storms. However, there are significant variabilities in the rainfall structures among the sensitivity simulations, except during the first 24-h spinup period. Specifically, the CTL and NGP storms display three different accumulated rainfall patterns: highly asymmetric with heavier (little) rainfall on the northeast (west) of the track in the first 84 h, more symmetric across the storm track afterwards, and two peak rainfall belts on both sides of the track with a minimum at the center in the last 12-h simulation. Of interest is that the third rainfall pattern occurs at the weakening stage of all the storms (strong or weak) during which time they are embedded in a weak-sheared environment with near-axisymmetric radar reflectivity distribution.

Rogers et al. (2003) studied the mechanisms whereby the first two rainfall patterns develop during the evolution of the same hurricane, that is, Bonnie (1998). They found that the accumulated rainfall is symmetrically distributed across the track when the wind shear vector was across the storm track, and asymmetrically distributed when the shear vector is along the track. Our sensitivity simulations, given in Fig. 11, appear to indicate that the storm intensity, vertical wind shear, and cloud microphysics processes all play important roles in determining the precipitation patterns. For example, in NEVP, the heaviest rainfall shifts from the northeast to the west of the track during the 24–72-h period, which is consistent with the distribution of the simulated reflectivity at 48 h (cf. Figs. 9b, 10b, and 11b). Such a shift does not appear in all the other weaker storms (cf. Figs. 11a–e). Subsequently, the azimuthal precipitation distribution becomes nearly axisymmetric, except to the south, leading to the symmetric rainfall pattern with a minimum at the center. This third rainfall pattern occurs much earlier than that in the other weak storms. An exception is the NMLT storm in which distinct rainfall maxima, with the heaviest accumulation among all the simulations, occur on the northeast of the track during the first 3 days, and then quickly shifts to the third rainfall pattern (Fig. 11c). This distinct rainfall structure and amount appear to result from the more rapid fallout of graupel due to the absence of melting, and the suppression of graupel production by the westerly descending inflows in the western eyewall. The rapid fallout also helps reduce water loading and facilitate the growth of updrafts and latent heat release (cf. Figs. 11c and 8). In both the NEVP and NMLT cases, pronounced rainfall begins to occur in the

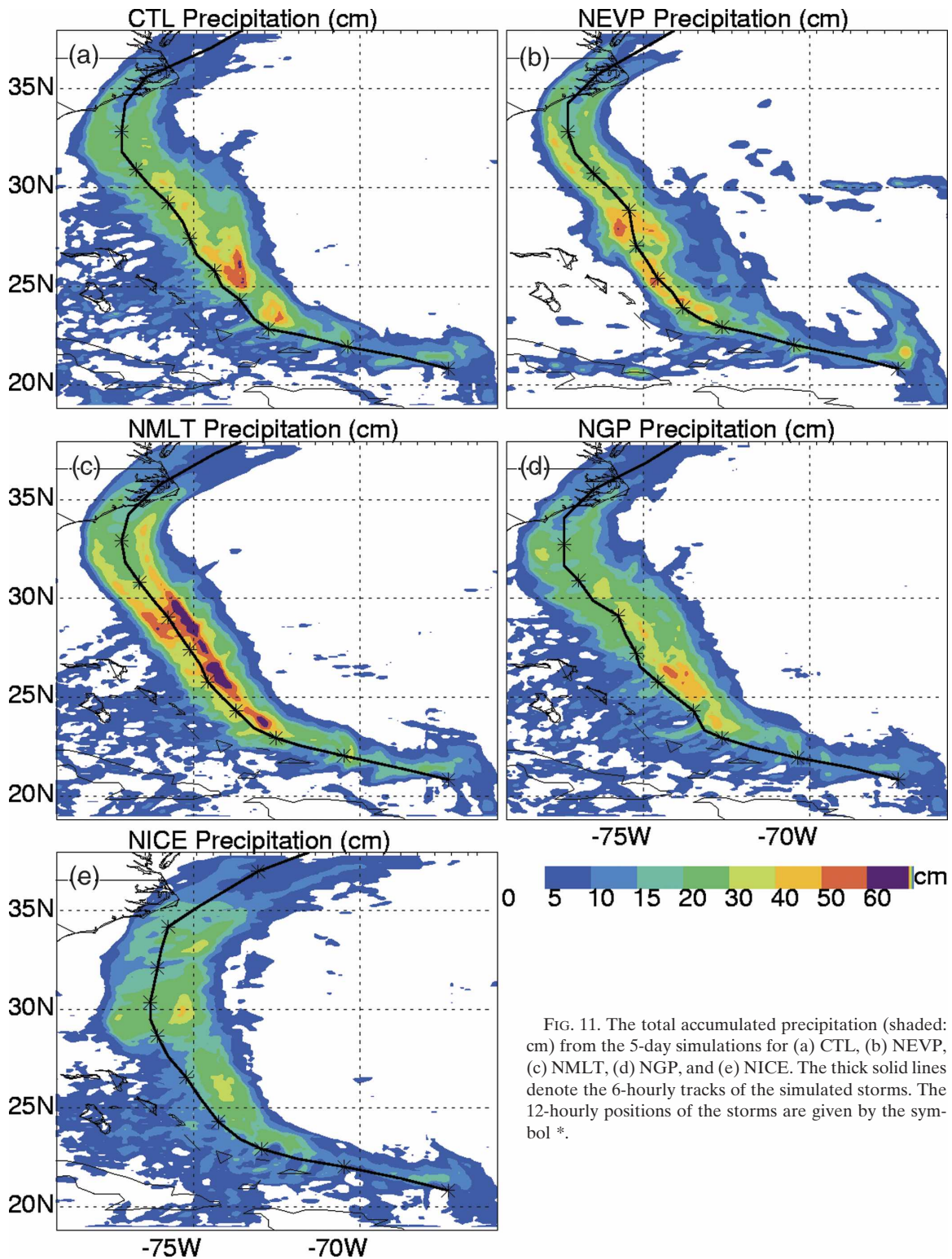


FIG. 11. The total accumulated precipitation (shaded: cm) from the 5-day simulations for (a) CTL, (b) NEVP, (c) NMLT, (d) NGP, and (e) NICE. The thick solid lines denote the 6-hourly tracks of the simulated storms. The 12-hourly positions of the storms are given by the symbol *.

western eyewall after 24 h, but 60 h in CTL and NGP, and 72 h in NICE. Again, this is because stronger hurricanes are less vulnerable to the influence of a vertical sheared environment. In view of many uncertainties in

our understanding and parameterizing cloud microphysics processes, the above results indicate the importance of validating and improving cloud microphysics parameterizations in order to improve the forecasts of

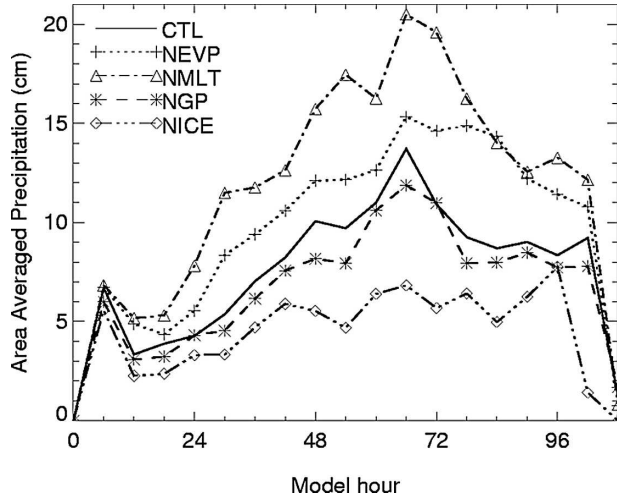


FIG. 12. The 6-hourly time series of the accumulated precipitation (cm) that is integrated within a radius of 100 km from the eye center from all five simulations.

intensity and the associated quantitative precipitation of tropical cyclones.

The 6-hourly time series of the storm-integrated rainfall is given in Fig. 12, which shows a reasonable correlation between the rainfall amount and storm intensity between different simulations. The NMLT storm is an exception, in which the greatest rainfall amount is produced, despite its weaker intensity than the NEVP storm (cf. Figs. 7 and 12); similarly for the local rainfall maxima (see Fig. 11). As mentioned before, this scenario could be attributed to the more rapid fallout of graupel without undergoing significant evaporation in the subcloud layer in NMLT and its positive feedback to the latent heat release. An important result from the sensitivity simulations presented herein is that incorporating ice microphysics facilitates the production of cloud hydrometeors due partly to the Bergeron process and partly to the addition of latent heat of fusion favoring the tropical cyclogenesis. Of interest is that precipitation continues to increase even 18 h after each storm ceases deepening at 48 h. This time lag appears to be caused by the increased fallout of hydrometeors in the vertical columns as the eyewall updrafts weaken.

Zhu et al. (2004) found the development of an eyewall replacement scenario in the CTL-simulated storm, in which its intensity weakens first and then begins to deepen, which is consistent with the previous observational finding (e.g., Willoughby et al. 1982). Similar eyewall replacement scenarios, albeit in different extents, also appear at the different timings of the storm development in all the sensitivity simulations, after moving into weak-sheared environments. Because of the limited space, we will present two different representative

scenarios of the eyewall replacement: one occurring in NGP and the other in NEVP. Figure 13a shows the time evolution of the simulated reflectivity and azimuthal winds in the NGP storm that is similar to, though much less evident and occurring earlier than, that in the CTL storm. That is, an outer rainband and a secondary wind maximum begin to develop at $R = \pm 170$ km in the western and eastern semicircles after 60 h into the integration. As a result of blocking the inward energy supply in the PBL, the eyewall convection weakens subsequently, like in the CTL storm (cf. Fig. 18 in Zhu et al. 2004 and Fig. 13a herein). Eventually, the outer rainband forms a new eyewall after the inner eyewall diminishes, completing an eyewall replacement cycle. A vertical cross section at $t = 69$ h shows the development

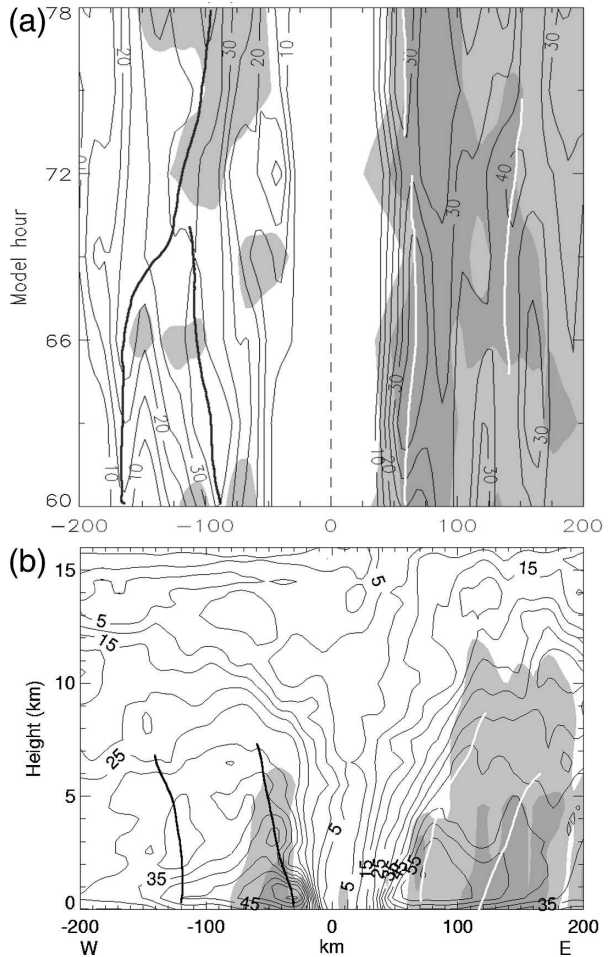


FIG. 13. (a) Time and west-east cross section of the horizontal wind speed at intervals of 5 m s^{-1} at $z = 3$ km from the 60–78-h NGP simulations, and (b) vertical (W–E) cross section of the horizontal wind speed at intervals of 5 m s^{-1} from the 69-h NGP simulation. Shadings denote the simulated radar reflectivity at 30 and 40 dBZ, and thick dashed lines denote the axes of the RMW.

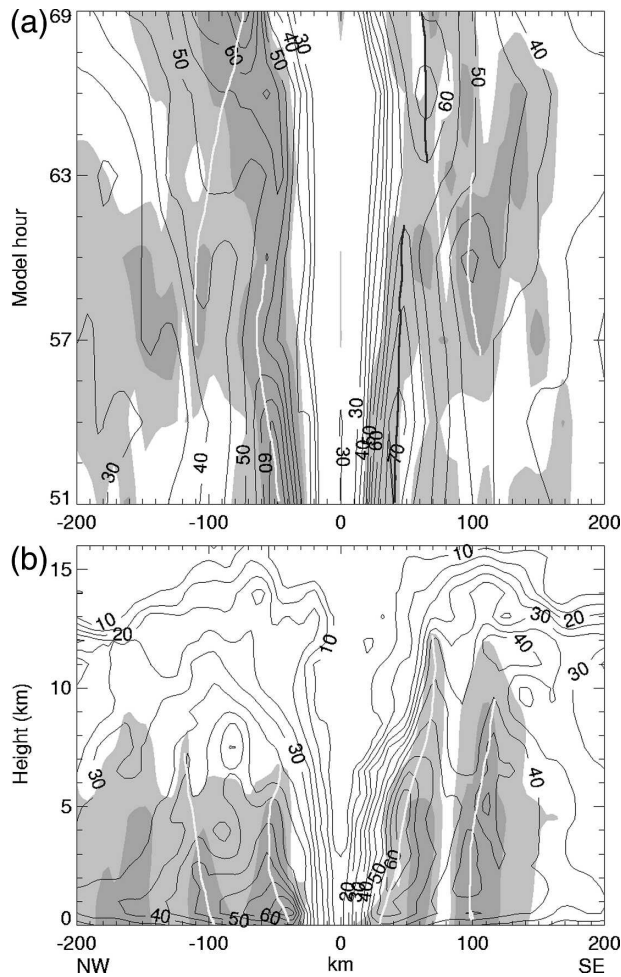


FIG. 14. As in Fig. 13 but for the NEVP storm: (a) from the 51–69-h simulations, and (b) from the 60-h simulation.

of the double eyewalls with two radially local wind maxima, although the outer-eyewall convection in the western quadrant is not strong at this time (Fig. 13b). The decrease of the maximum wind speed of the inner eyewall from 60 to 72 h and the subsequent eyewall replacement are consistent with the central pressure fall, followed by a filling of the storm (cf. Figs. 13a and 7). Such eyewall replacement structures are much less organized in weaker storms, such as in NGP and NICE (not shown).

In contrast, the NEVP storm exhibits the development of a weaker rainband and a secondary wind maximum near $R = -200$ km at $t = 51$ h (Fig. 14a). Of interest is that their radius shrinks with time until 66 h when they merge with the RMW in the eyewall at $R = -60$ km. Meanwhile, the intense rotational winds in the eyewall weaken from 68 m s^{-1} at 51 h to 52 m s^{-1} at 60 h while their radius expands outward without losing their characters. Clearly, these structural changes differ

from those in the NGP and CTL storms (cf. Figs. 13a and 14a). Although they remain to be validated by observations, the inner eyewall in NEVP does not weaken as rapidly as in NGP or CTL likely because the outer rainband is relatively too weak to block the energy supply to intensify the inner eyewall updrafts. Nevertheless, the above mentioned CTL and NGP scenarios appear more or less in the southeast semicircle of the NEVP storm (Fig. 14a). Of importance is that the inner-core structural changes in NEVP coincide well to a period of rapid weakening (i.e., 20 hPa in P_{\min}) from 48 to 60 h, followed by a period of slow deepening from 60 to 72 h of the storm (cf. Figs. 14a and 7). The double eyewalls with secondary wind maxima could be clearly seen up to $z = 10$ km from a vertical cross section of the azimuthal winds and reflectivity at 60 h (see Fig. 14b). As in the CTL simulation, the double eyewall structures could only be maintained for a period of about 6 h. The results indicate that the eyewall replacement processes are determined by the large-scale sheared flows rather than by the cloud microphysics processes, but their associated structural changes could differ from storm to storm, depending on their intensity and latent heat release (or cloud microphysics). The eyewall replacement would be less evident and has less impact on the intensity changes when hurricanes are weak.

5. Summary and conclusions

In this study, five sensitivity simulations with varying cloud microphysics processes are conducted, using the results presented in Part I (Zhu et al. 2004) as a control (CTL) run, to examine the effects of ice microphysics processes on the simulation of hurricane intensity and intensity changes, and the development of asymmetric cloud/precipitation structures as well as the eyewall replacement scenarios. All sensitivity simulations are integrated for 5 days using the nested-grid, cloud-resolving version of the PSU–NCAR Mesoscale Model (i.e., MM5) with the finest grid size of 4 km.

In general, the model-simulated hurricane track exhibits little sensitivity to varying cloud physical processes, except for the weakest and shallowest storm (i.e., NICE) that differs markedly from the CTL storm because of its turning too early to the northeast. The result suggests that weaker and shallower storms are more influenced in track by the large-scale flow. However, varying cloud physics processes cloud cause pronounced sensitivities in hurricane intensity and inner-core structures with respect to the CTL storm, starting from 24 h into the integration; their extreme amplitudes range from 50 hPa (or 20 m s^{-1}) overdeepening to 15 hPa (or 12 m s^{-1}) underdeepening in the minimum surface pressure (maximum surface wind). Specifically,

- When all the (three class) ice microphysics processes are removed (NICE), the model produces the weakest and shallowest storm among all the sensitivity simulations because of the neglect of the important Bergeron processes, including the growth and rapid fallout of graupel in the eyewall updrafts, and the latent heat of fusion. The NICE storm is characterized with widespread cloud water but little rainwater in the upper troposphere because of the absence of the latent heat release of fusion and the initiation of cloud ice for $T < 0^{\circ}\text{C}$. Most of the latent heating and cloud hydrometeors production occur in the lowest 5 km.
- In the absence of graupel (NGP), the model produces a slightly weaker storm with less precipitation. The NGP storm exhibits too much concentration of ice particles above the melting level, and a wider lateral size of and more extensive clouds in the eyewall. They are likely caused by the fact that snow can be advected more horizontally than vertically relative to graupel. A comparison between the CTL and NGP storms suggests that the presence of graupel helps narrow the lateral eyewall size due to its rapid fallout with respect to snow, and the added latent heat of fusion (reduced water loading) plays a primary (secondary) role in intensifying the eyewall updrafts. Moreover, it could enhance the latent heat release of fusion due to its faster depositional growth relative to snow. The water loading effect appears to be more significant during the mature stage of a hurricane.
- Without the evaporation of cloud water and rainwater (NEVP), the model produces the deepest storm with the smallest RMW, a wider eyewall, and the strongest eyewall updrafts. This rapid development appears to result from a positive feedback between the low-level warm-air convergence, the latent heat release in the eyewall, and surface pressure falls. Similar storm intensity but the most rainfall is simulated when the melting effect is ignored (NMLT). The results indicate the important roles of melting and evaporative cooling in braking the amplification and determining the final intensity of tropical cyclones. Vertical heating profiles show that the melting cooling is more pronounced in the eyewall where a tremendous amount of frozen hydrometeors, particularly graupel, is present, whereas the evaporative cooling occurs more markedly when the storm environment is more unsaturated.
- Although the control-simulated wavenumber-1 cloud asymmetries develop in all the sensitivity simulations, stronger storms (e.g., NEVP and NMLT) tend to have more intense and compact eyewall updrafts, and produce heavier precipitation with more clouds dis-

tributed (or less cloud-free) in the western half of the eyewall due to the more rapid rotational advection of cloud hydrometeors. In contrast, weaker storms (e.g., NICE and NGP) are less organized, more asymmetric in the vertical structure with the minimum central pressure axis (and the RMW and the warm-cored eye) tilting downshear. The results indicate that weaker storms are more vulnerable to the influence of larger-scale sheared flows that, in the present case, play an important role in suppressing cloud and precipitation in the west semicircle of the eyewall. It is shown that the peak rainfall rates may lag 6–12 h behind the timing of the maximum intensity.

- It is found that although the eyewall replacement scenarios, often occurring in weak-sheared environments, could develop at the different timings of all the sensitivity simulations, their associated inner-core structural changes differ significantly, depending on the storm intensity. For relatively weaker storms, the inner eyewall convection diminishes after an outer rainband and a secondary wind maximum develop and block the inward energy supply. The outer rainband then forms a new eyewall, completing an eyewall replacement cycle. By comparison, the outer rainband in stronger storms does not have detrimental impact on the eyewall convection, but they tend to be merged into one new eyewall with a different RMW. Nevertheless, the eyewall replacement cycle is seen closely related to the simulated hurricane intensity changes.

Based on the above results, we may conclude that varying cloud microphysics processes could affect not only the intensity and intensity changes of the simulated tropical cyclones, but also their inner-core structural changes and associated clouds and precipitation under the influence of large-scale sheared flows. In view of the pronounced sensitivity of ice microphysics, this work suggests that more future research effort be focused on the validation and improvement of the current ice microphysics parameterizations, particularly the processes occurring in the melting/freezing layer, in order to improve the numerical prediction of the hurricane intensity, intensity changes and associated precipitation. It should be mentioned that some inner-core structural changes and their associated timing and location, described in this work, may differ, for example, during the eyewall replacement, when higher grid resolutions are used.

Acknowledgments. The authors wish to thank Dr. Fu-Zhong Weng for his interest and support of this research. This work was supported by NASA Grants

NAG-57842 and NAG-510746, NSF Grants ATM-9802391 and ATM-0342363, and ONR Grant N000140210402.

REFERENCES

- Avila, L. A., 1998: Hurricane Bonnie preliminary report 19–30 August 1998. National Hurricane Center, 10 pp. [Available online at <http://www.nhc.noaa.gov/1998bonnie.html>.]
- Braun, S. A., and W.-K. Tao, 2000: Sensitivity of high-resolution simulations of Hurricane Bob (1991) to planetary layer parameterizations. *Mon. Wea. Rev.*, **128**, 3941–3961.
- Brown, J. M., 1979: Mesoscale unsaturated downdraft driven by rainfall evaporation: A numerical study. *J. Atmos. Sci.*, **36**, 313–338.
- Chelton, D. B., F. J. Wentz, C. L. Gentemann, R. A. de Szoeke, and M. G. Schlax, 2000: Satellite microwave SST observations of transequatorial tropical instability waves. *Geophys. Res. Lett.*, **27**, 1239–1242.
- Dudhia, J., 1993: A nonhydrostatic version of the Penn State–NCAR mesoscale model: Validation tests and simulation of an Atlantic cyclone and cold front. *Mon. Wea. Rev.*, **121**, 1493–1513.
- Fujita, T., 1959: Precipitation and cold-air production in mesoscale thunderstorm systems. *J. Meteor.*, **16**, 454–466.
- Grell, G. A., J. Dudhia, and D. R. Stauffer, 1995: A description of the fifth generation Penn State/NCAR Mesoscale Model (MM5). NCAR Tech. Note NCAR/TN-398+STR, 138 pp. [Available from NCAR Publications Office, P.O. Box 3000, Boulder, CO 80307-3000.]
- Leary, C. A., and R. A. Houze Jr., 1979: Melting and evaporation of hydrometeors in precipitation from anvil clouds of deep tropical convection. *J. Atmos. Sci.*, **36**, 669–679.
- Liu, Y., D.-L. Zhang, and M. K. Yau, 1997: A multiscale numerical study of Hurricane Andrew (1992). Part I: Explicit simulation and verification. *Mon. Wea. Rev.*, **125**, 3073–3093.
- , —, and —, 1999: A multiscale numerical study of Hurricane Andrew (1992). Part II: Kinematics and inner-core structures. *Mon. Wea. Rev.*, **127**, 2597–2616.
- Lord, S. J., H. E. Willoughby, and J. M. Piotrowicz, 1984: Role of a parameterized ice-phase microphysics in an axisymmetric tropical cyclone model. *J. Atmos. Sci.*, **41**, 2836–2848.
- McCumber, M., W.-K. Tao, and J. Simpson, 1991: Comparison of ice-phase microphysical parameterization schemes using numerical simulation of tropical convection. *J. Appl. Meteor.*, **30**, 985–1004.
- Montgomery, M. T., and R. J. Kallenbach, 1997: A theory for vortex Rossby-waves and its application to spiral bands and intensity changes in hurricanes. *Quart. J. Roy. Meteor. Soc.*, **123**, 435–465.
- Riehl, H., 1969: Some aspects of cumulonimbus convection in relation to tropical weather system. *Bull. Amer. Meteor. Soc.*, **50**, 587–595.
- Rogers, R., S. Chen, J. Tenerelli, and H. Willoughby, 2003: A numerical study of the impact of vertical shear on the distribution of rainfall in Hurricane Bonnie (1998). *Mon. Wea. Rev.*, **131**, 1577–1599.
- Rosenthal, S. L., 1978: Numerical simulation of tropical cyclone development with latent heat release by resolvable scales. I: Model description and preliminary results. *J. Atmos. Sci.*, **35**, 258–271.
- Simpson, J., R. H. Simpson, D. A. Andrews, and M. A. Eaton, 1965: Experimental cumulus dynamics. *Rev. Geophys.*, **3**, 387–431.
- Tao, W.-K., and J. Simpson, 1993: the Goddard cumulus ensemble model. Part I: Model description. *Terr. Atmos. Oceanic Sci.*, **4**, 35–72.
- Wang, Y., 2001: An explicit simulation of tropical cyclones with a triply nested movable mesh primitive equation model: TCM3. Part I: Description of the model and control experiment. *Mon. Wea. Rev.*, **129**, 1270–1294.
- , 2002: An explicit simulation of tropical cyclones with a triply nested movable mesh primitive equation model: TCM3. Part II: Model refinements and sensitivity to cloud microphysics parameterization. *Mon. Wea. Rev.*, **130**, 3022–3036.
- Willoughby, H. E., 1978: A possible mechanism for the formation of hurricane rainbands. *J. Atmos. Sci.*, **35**, 838–848.
- , J. A. Clos, and M. G. Shoreibah, 1982: Concentric eye walls, secondary wind maxima, and the evolution of the hurricane vortex. *J. Atmos. Sci.*, **39**, 395–411.
- , H.-L. Jin, S. J. Lord, and J. M. Piotrowicz, 1984: Hurricane structure and evolution as simulated by an axisymmetric, nonhydrostatic numerical model. *J. Atmos. Sci.*, **41**, 1169–1186.
- Yamasaki, M., 1977: A preliminary experiment of the tropical cyclone without parameterizing the effects of cumulus convection. *J. Meteor. Soc. Japan*, **55**, 11–30.
- Yau, M. K., Y. Liu, D.-L. Zhang, and Y. Chen, 2004: A multiscale numerical study of Hurricane Andrew (1992). Part VI: Small-scale inner-core structures and wind streaks. *Mon. Wea. Rev.*, **132**, 1410–1433.
- Zhang, D.-L., 1989: The effect of parameterized ice microphysics on the simulation of vortex circulation with a mesoscale hydrostatic model. *Tellus*, **41A**, 132–147.
- , 1998: The effects of diabatic physical processes on the simulations of mesoscale convective systems. *Chinese J. Atmos. Sci.*, **22**, 435–451.
- , and R. A. Anthes, 1982: A high-resolution model of the planetary boundary layer—Sensitivity tests and comparisons with SESAME-79 data. *J. Appl. Meteor.*, **21**, 1594–1609.
- , and J. M. Fritsch, 1988: Numerical sensitivity experiments of varying model physics on the structure, evolution and dynamics of two mesoscale convective systems. *J. Atmos. Sci.*, **45**, 261–293.
- , and K. Gao, 1989: Numerical simulation of an intense squall line during 10–11 June PRESTORM. Part II: Rear inflow, surface pressure perturbations and stratiform precipitation. *Mon. Wea. Rev.*, **117**, 2067–2094.
- , J. S. Kain, J. M. Fritsch, and K. Gao, 1994: Comments on “Parameterization of convective precipitation in mesoscale numerical models: A critical review.” *Mon. Wea. Rev.*, **122**, 2222–2231.
- , Y. Liu, and M. K. Yau, 2000: A multiscale numerical study of Hurricane Andrew (1992). Part III: Dynamically induced vertical motion. *Mon. Wea. Rev.*, **128**, 3772–3788.
- , —, and —, 2002: A multiscale numerical study of Hurricane Andrew (1992). Part V: Inner-core thermodynamics. *Mon. Wea. Rev.*, **130**, 2745–2763.
- Zhu, T., D.-L. Zhang, and F. Weng, 2002: Impact of the advanced microwave sounding unit measurements on hurricane prediction. *Mon. Wea. Rev.*, **130**, 2416–2432.
- , —, and —, 2004: Numerical simulation of Hurricane Bonnie (1998). Part I: Model verification and evolution of the eyewall. *Mon. Wea. Rev.*, **132**, 225–241.
- Zipser, E. J., 1969: The role of organized unsaturated downdrafts in the structure and rapid decay of an equatorial disturbance. *J. Appl. Meteor.*, **8**, 799–814.

Copyright of *Journal of the Atmospheric Sciences* is the property of *American Meteorological Society* and its content may not be copied or emailed to multiple sites or posted to a listserv without the copyright holder's express written permission. However, users may print, download, or email articles for individual use.